The Predictive Power of Computational Astrophysics as a Discovery Tool
Proceedings IAU Symposium No. 362, 2023
D. Bisikalo, D. Wiebe & C. Boily, eds.
doi:10.1017/S1743921322001314

A New Code for Relativistic Hydrodynamics and its Application to FR II Radio Jets

Jeongbhin Seo[1], Hyesung Kang[1] and Dongsu Ryu[2]

[1]Department of Earth Sciences, Pusan National University, Busan 46241, Korea

[2]Department of Physics, UNIST, Ulsan, 44919, Korea

Abstract. To study the dynamics of relativistic flows in astrophysical objects such as radio jets, we have developed a new special relativistic hydrodynamic (RHD) code based on the weighted essentially non-oscillatory (WENO) scheme, a high-order finite difference scheme. The code includes different WENO versions, and high-order time integration methods such as the 4th-order accurate Runge-Kutta (RK4) and strong stability preserving RK (SSPRK), as well as the equations of state (EOSs) that closely approximate the EOS of the single-component perfect gas in relativistic regime. Additionally, it is optimized for the reproduction of complex structures in multi-dimensional flows, and implements a modification of eigenvalues for the acoustic modes to effectively control carbuncle instability. As the first application of the code, we have simulated ultra-relativistic jets of FR II radio galaxies, and studied the nonlinear flow structures, such as shocks, velocity shear, and turbulence, through large-scale.

Keywords. hydrodynamics, galaxies: jets, methods: numerical, relativistic processes

1. Introduction

Relativistic jets are widely involved in high-energy astrophysical phenomena, such as, pulsar wind nebulae (PWNs), gamma-ray bursts (GRBs), and radio-loud active galactic nuclei (AGNs) (see Hardcastle & Croston 2020, for reviews). Many studies of relativistic jets have been done through relativistic hydrodynamics (RHD) simulations (English et al. 2016; Li et al. 2018; Matthews et al. 2019). Those studies adopted various codes that were developed from non-relativistic Newtonian hydrodynamics codes (see Martí & Müller 2003, 2015, for reviews). A popular numerical scheme for these codes is the weighted essentially non-oscillatory (WENO) scheme based on the upwind method, which is designed to achieve a high-order accuracy in smooth flows and avoid spurious oscillations near discontinuities, e.g., shocks and contact discontinuities. The first WENO scheme was introduced by Liu et al. (1994), which is a finite volume (FV) scheme. Later, a 5th-order accurate, finite difference (FD) WENO scheme was introduced by Jiang & Shu (1996), where the fluxes at the cell interfaces are reconstructed using the point values of the physical fluxes with weight functions. After that, different FD WENO versions have been proposed, achieving higher accuracies for smooth flows and/or smaller dissipation near discontinuities. We have developed a new code based on the WENO scheme, including three versions of WENO, WENO-JS (Jiang & Shu 1996), WENO-Z (Borges et al. 2008), and WENO-ZA (Liu et al. 2018).

The WENO scheme has been combined with high-order time integration methods, such as the classical Runge-Kutta (RK) method (e.g., Shu & Osher 1988, 1989; Jiang & Shu 1996). To enhance the nonlinear stability and reduce spurious oscillations near discontinuous structures, Spiteri & Ruuth (2002) introduced an improved RK, called

the strong-stability-preserving Runge-Kutta (SSPRK) method. Our code includes the 4th-order accurate RK and SSPRK time integration methods.

In terms of thermodynamics, fluids that have thermal speeds approaching the speed of light manifest relativistic effects. In our code, we consider the equation of state (EOS) for "single-component" fluids. The EOS of the single-component, perfect gas, called RP (relativistic perfect) here, contains modified Bessel functions, which are difficult to be efficiently implemented in numerical codes (e.g., Synge et al. 1957). Hence, RHD simulations have been performed typically with simplified EOSs. The most popular EOS is the ID (ideal) EOS, which assumes a constant adiabatic index γ. However, the ID EOS cannot reproduce the transition from subrelativistic temperature of $\Theta \equiv p/\rho c^2 < 1$ to fully relativistic temperature of $\Theta > 1$. Here, Θ, p, and ρ are a temperature-like variable, the isotropic gas pressure, and the rest mass density, respectively. On the other hand, EOSs that closely approximate RP have been introduced, including TM (after Taub-Mathews, see Taub 1948; Mathews 1971; Mignone et al. 2006) and RC (after Ryu-Chattopadhyay, see Ryu et al. 2006). Our code contains these EOSs, as well as the ID EOS.

For multi-dimensional problems, the high-order accuracy in FD schemes can be preserved with the dimension-by-dimension method. Recently, Buchmüller & Helzel (2014) and Buchmüller et al. (2016) proposed a modified dimension-by-dimension method that implements the averaging of the state and flux vectors along the transverse direction, and demonstrated higher accurate reproduction of complex, nonlinear multi-dimensional structures. We adopt this method in our code.

It is know that the Carbuncle instability, which deforms grid-aligned, slow-moving shocks, is easily generated in high-accuracy, shock-capturing, upwind codes (e.g., Peery et al. 2018; Dumbser et al. 2008). This instability appears due to the insufficient numerical dissipation at such shocks. Fleischmann et al. (2020) introduced a method which efficiently mitigates the carbuncle instability by modifying eigenvalues for the acoustic modes. Our code includes this fix, as well.

Using our RHD code, we have simulated ultra-relativistic jets injected into the intracluster medium, with the parameters relevant to FR-II radio galaxies. In this paper, we briefly describe the code and also the flow structures in a FR II jet, such as, shocks, shear, and turbulence. The complete description of the code and jet simulations can be found in Seo et al. (2021a) and Seo et al. (2021b).

2. Description of the Code

2.1. *RHD Equations*

The code solves the conservation equations of special relativistic hydrodynamics, which are expressed in the laboratory frame as,

$$\frac{\partial D}{\partial t} + \vec{\nabla} \cdot (D\vec{v}) = 0, \tag{2.1}$$

$$\frac{\partial \vec{M}}{\partial t} + \vec{\nabla} \cdot (\vec{M}\vec{v} + p) = 0, \tag{2.2}$$

$$\frac{\partial E}{\partial t} + \vec{\nabla} \cdot [(E + p)\vec{v}] = 0. \tag{2.3}$$

Here, the conserved quantities, the mass, momentum, and total energy densities, are given as $D = \Gamma\rho$, $\vec{M} = \Gamma^2\rho(h/c^2)\vec{v}$, and $E = \Gamma^2\rho h - p$, respectively (e.g Landau & Lifshitz 1959), where c, ρ, $\vec{v}$, p, Γ, and h are the speed of light, the rest mass density, the fluid three-velocity, the isotropic gas pressure, the Lorentz factor, and the specific enthalpy.

https://doi.org/10.1017/S1743921322001314 Published online by Cambridge University Press

2.2. *Equation of State*

The EOS of the single-component, perfect gas, RP, is given as

$$h(p,\rho)=\frac{K_3(1/\Theta)}{K_2(1/\Theta)}, \tag{2.4}$$

where K_α is the modified Bessel function of the second kind of order α (e.g., Synge et al. 1957). As h contains Bessel functions, the inversion of the conserved quantities to get the primitive variables, ρ, $\vec{v}$, and p, is computationally expensive. Here, we list three approximate EOSs, ID, TM, and RC, implemented in the code, respectively:

$$h=1+\frac{\gamma\Theta}{\gamma-1},\quad h=\frac{5}{2}\Theta+\frac{3}{2}\sqrt{\Theta^2+\frac{4}{9}},\quad h=2\frac{6\Theta^2+4\Theta+1}{3\Theta+2}, \tag{2.5}$$

where γ is the adiabatic index. As mentioned in the introduction, ID cannot treat the transition from subrelativistic to fully relativistic. According to Ryu et al. (2006), RC reproduces RP slightly better than TM, so we have adopted RC in our jet simulations.

2.3. *Spatial Integration*

By using the dimension-by-dimension method in Cartesian geometry, Equations (2.1) - (2.3) are solved numerically, as follows,

$$\begin{aligned}\boldsymbol{q}'_{i,j,k}=\boldsymbol{q}_{i,j,k}&-\frac{\Delta t}{\Delta x}\left(\boldsymbol{F}_{i+\frac{1}{2},j,k}-\boldsymbol{F}_{i-\frac{1}{2},j,k}\right)\\&-\frac{\Delta t}{\Delta y}\left(\boldsymbol{G}_{i,j+\frac{1}{2},k}-\boldsymbol{G}_{i,j-\frac{1}{2},k}\right)-\frac{\Delta t}{\Delta z}\left(\boldsymbol{H}_{i,j,k+\frac{1}{2}}-\boldsymbol{H}_{i,j,k-\frac{1}{2}}\right),\end{aligned} \tag{2.6}$$

where q, F, G, and H are the state vector and the flux vectors along the x, y, and z-directions. Here, i, j, and k are the grid indices along the x, y, and z-directions, and the unprimed and primed quantities are defined at t and $t+\Delta t$, respectively. The 5th-order accurate FD WENO scheme is used to estimate the cell interface fluxes, $\boldsymbol{F}_{i\pm\frac{1}{2},j,k}$, $\boldsymbol{G}_{i,j\pm\frac{1}{2},k}$, and $\boldsymbol{H}_{i,j,k\pm\frac{1}{2}}$, (see Jiang & Wu 1999, for detail). The code includes three versions of WENO, the original WENO-JS of Jiang & Shu (1996), and WENO-Z (Borges et al. 2008) and WENO-ZA (Liu et al. 2018), both of which are designed to improve the performance over the original WENO-JS. We have tested the three variants with various RHD test problems. While WENO-JS is the most stable in various conditions, it gives the most diffusive solutions. On the other hand, WENO-ZA gives less diffusive solutions, but they often break down when there are steep gradients. We have found that WENO-Z is best fitted because of its balance between stability and accuracy, and hence we employed it for our jet simulations.

2.4. *Time Integration*

The 4th-order RK method has been commonly used with the 5th-order WENO scheme (e.g., Shu & Osher 1988, 1989; Jiang & Shu 1996). Its time-stepping from $\boldsymbol{q}^n$ to $\boldsymbol{q}^{n+1}$ is given as

$$\begin{aligned}&\boldsymbol{q}^{(0)}=\boldsymbol{q}^n,\quad \boldsymbol{q}^{(1)}=\boldsymbol{q}^{(0)}+\frac{\Delta t}{2}\boldsymbol{\mathcal{L}}^{(0)},\quad \boldsymbol{q}^{(2)}=\boldsymbol{q}^{(0)}+\frac{\Delta t}{2}\boldsymbol{\mathcal{L}}^{(1)},\\&\boldsymbol{q}^{(3)}=\boldsymbol{q}^{(0)}+\Delta t\boldsymbol{\mathcal{L}}^{(2)},\quad \boldsymbol{q}^{n+1}=\frac{1}{3}\left(-\boldsymbol{q}^{(0)}+\boldsymbol{q}^{(1)}+2\boldsymbol{q}^{(2)}+\boldsymbol{q}^{(3)}\right)+\frac{\Delta t}{6}\boldsymbol{\mathcal{L}}^{(3)}.\end{aligned} \tag{2.7}$$

https://doi.org/10.1017/S1743921322001314 Published online by Cambridge University Press

Here, n is the timestep. In the 4th-order accurate, 5-stage SSPRK method (e.g., Spiteri & Ruuth 2002, 2003; Gottlieb 2005), the time-stepping is given as

$$\boldsymbol{q}^{(0)} = \boldsymbol{q}^n, \qquad \boldsymbol{q}^{(l)} = \sum_{m=0}^{l-1} (\chi_{lm}\boldsymbol{q}^{(m)} + \Delta t \beta_{lm}\boldsymbol{\mathcal{L}}^{(m)}), \quad l = 1, 2, \cdots, 5, \qquad \boldsymbol{q}^{n+1} = \boldsymbol{q}^{(5)}, \tag{2.8}$$

where $\boldsymbol{\mathcal{L}}^{(l)}_{i,j,k}$ is

$$\boldsymbol{\mathcal{L}}^{(l)}_{i,j,k} = -\frac{\boldsymbol{F}^{(l)}_{i+\frac{1}{2},j,k} - \boldsymbol{F}^{(l)}_{i-\frac{1}{2},j,k}}{\Delta x} - \frac{\boldsymbol{G}^{(l)}_{i,j+\frac{1}{2},k} - \boldsymbol{G}^{(l)}_{i,j-\frac{1}{2},k}}{\Delta y} - \frac{\boldsymbol{H}^{(l)}_{i,j,k+\frac{1}{2}} - \boldsymbol{H}^{(l)}_{i,j,k-\frac{1}{2}}}{\Delta z}, \tag{2.9}$$

χ_{lm} and β_{lm} are the coefficients (Spiteri & Ruuth 2002).

For the stability in time integration, the time step, Δt, is restricted by the so-called Courant-Friedrichs-Levy (CFL) condition,

$$\Delta t = \mathrm{CFL} / \left[\frac{\lambda_x^{\max}}{\Delta x} + \frac{\lambda_y^{\max}}{\Delta y} + \frac{\lambda_z^{\max}}{\Delta z} \right], \tag{2.10}$$

where $\lambda^{\max}$'s are the maxima of the cell-centered eigenvalues. We use CFL=0.8 in our code, which seems to be a good compromise for stability and speed. RK4 and SSPRK give similar results in tests of moderate RHD problems, but in the shock tests where the initial velocity perpendicular to the shock normal, $v_\perp$, is close to c, SSPRK gives more stable solutions than RK4. In relativistic jets, strong shears appear across the jet and backflows, and shocks with large $v_\perp$ could form, so we use SSPRK for the time integration.

2.5. *Averaging of Fluxes along Transverse Directions*

Our code includes transverse-flux averaging in the stage of the calculation of WENO fluxes, which improves the performance of multi-dimensional problems. The 4th-order accurate averaging scheme, given as (Buchmüller & Helzel 2014; Buchmüller et al. 2016),

$$\bar{\boldsymbol{q}}_{i,j,k} = \boldsymbol{q}_{i,j,k} - \frac{1}{24}\left(\boldsymbol{q}_{i,j-1,k} - 2\boldsymbol{q}_{i,j,k} + \boldsymbol{q}_{i,j+1,k}\right) - \frac{1}{24}\left(\boldsymbol{q}_{i,j,k-1} - 2\boldsymbol{q}_{i,j,k} + \boldsymbol{q}_{i,j,k+1}\right), \tag{2.11}$$

and

$$\begin{aligned}\bar{\boldsymbol{F}}_{i\pm\frac{1}{2},j,k} = \boldsymbol{F}_{i\pm\frac{1}{2},j,k} &+ \frac{1}{24}\left(\boldsymbol{F}_{i\pm\frac{1}{2},j-1,k} - 2\boldsymbol{F}_{i\pm\frac{1}{2},j,k} + \boldsymbol{F}_{i\pm\frac{1}{2},j+1,k}\right) \\ &+ \frac{1}{24}\left(\boldsymbol{F}_{i\pm\frac{1}{2},j,k-1} - 2\boldsymbol{F}_{i\pm\frac{1}{2},j,k} + \boldsymbol{F}_{i\pm\frac{1}{2},j,k+1}\right),\end{aligned} \tag{2.12}$$

is used. We have adopted this scheme that has the same order of accuracy as the time integration. We found that with this averaging, complex structures like vortices in the relativistic Kelvin-Helmholtz test are better reproduced (see Seo et al. 2021a).

2.6. *Suppression of Carbuncle Instability*

Low Mach number shocks that are aligned with the computational grid and move slowly are susceptible to carbuncle instability, owing to the lack of sufficient dissipation. Fleischmann et al. (2020) suggested that a modification of eigenvalues for two acoustic modes,

$$c_s' = \min(\phi|v_x|, c_s), \qquad \lambda_{1,5} = v_x \pm c_s', \tag{2.13}$$

could suppress this instability in Newtonian hydrodynamic codes. Here, ϕ is a positive number of order $\mathcal{O}(1)$. This method alleviates the instability problem by increasing the

https://doi.org/10.1017/S1743921322001314 Published online by Cambridge University Press

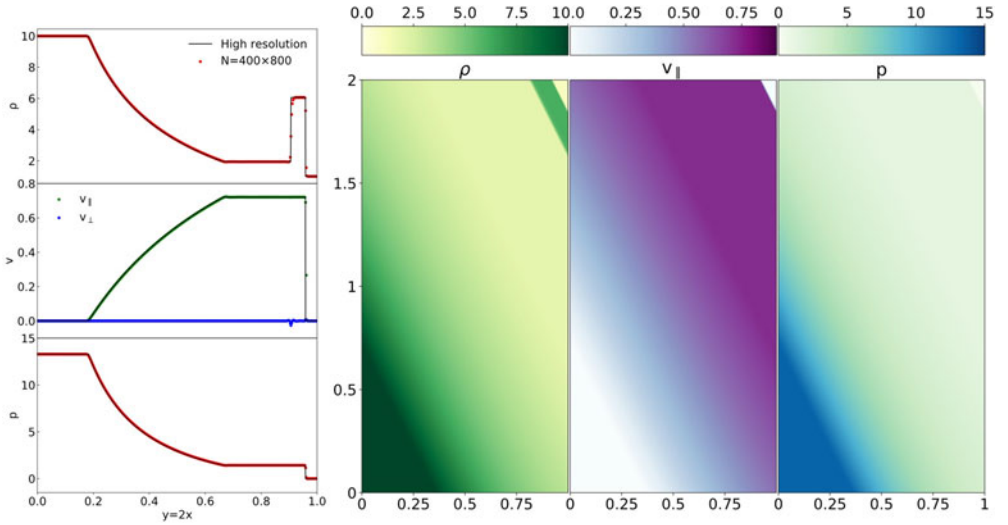

Figure 1. 2D relativistic shock tube test. The results of a simulation using 400×800 grid zones are shown $t = 0.45 \times \sqrt{5}$. *Left panels*: The flow quantities along $y = 2x$ (red dots) are compared to those from 1D high-resolution results with 20,000 grid zones for a converged benchmark (black solid lines). Here, $v_{\parallel}$ and $v_{\perp}$ are the velocity parallel and perpendicular to the normal of the shock and contact discontinuity, respectively. *Right panels*: The corresponding 2D images are shown.

acoustic Mach number to $M \geq 1/\phi$. We adopt this idea to our RHD code, modifying the eigenvalues of two acoustic modes as,

$$c'_s = \min(\phi|v_x|, c_s), \qquad \lambda_{1,5} = \frac{(1 - c'^2_s)v_x \pm c'_s/\Gamma\sqrt{\mathcal{Q}}}{1 - c'^2_s v^2}, \tag{2.14}$$

where $\mathcal{Q} = 1 - v_x^2 - c'^2_s(v_y^2 + v_z^2)$. In simulations of RHD jets, As shown in the Figure 9 of Seo et al. (2021a), a part of the bowshock may be subject to carbuncle instability. We have found that this modification efficiently suppresses the instability.

2.7. *Code test : 2D Relativistic Shock Tube*

As the verification of the code, we present the results of a two-dimensional (2D) shock tube test. The initial condition is given as $u_L = (10, 0, 0, 13.3)$ for $y < 2(1 - x)$ and $\boldsymbol{u}_R = (1, 0, 0, 10^{-6})$ for $y > 2(1 - x)$, where $\boldsymbol{u} = (\rho, v_x, v_y, p)$. As shown in Figure 1, the shock and contact discontinuity are resolved with $2 - 3$ cells, and the rarefaction wave are well reproduced. We also see that the velocity perpendicular to the normal of the shock and contact discontinuity, $v_{\perp}$, which is an indication of numerical error in this test, is small with $|v_{\perp}/v_{\parallel}| \approx 1 - 2\%$.

The full description of the code along with a number of tests is given in Seo et al. (2021a).

3. Application to FR II Jets

As the first application of our RHD code, we have simulated three-dimensional (3D) FR II jets, which have well collimated structures and bright heads. In Figure 2, we present the 2D slice distributions of the density and vertical velocity in one of the simulated jets. The length scale of the shown jet is about 60kpc with the jet radius of $r_j = 1$kpc. The jet power, the energy injection rate through the jet radius, is matched to the value of typical FR II jets, $Q \approx 3.34 \times 10^{46}$erg/s. We have found that our code well reproduces

https://doi.org/10.1017/S1743921322001314 Published online by Cambridge University Press

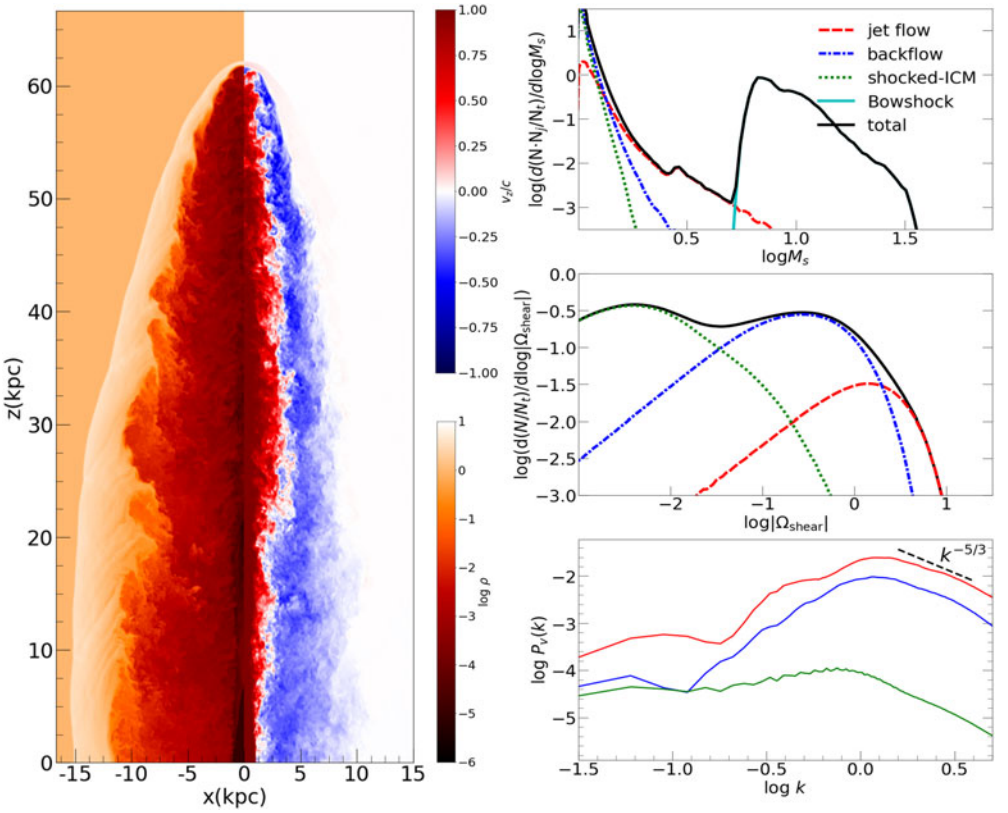

Figure 2. *left panels*: Density (left) and velocity(right) slice distributions at $t = 1.5$Myr in a FR II jet simulation with $(600)^2 \times 1200$ grid zones. *Right panels*: The PDF of the Mach number of the shocks generated in the jet-induced flow (top), the PDF of shear, $\Omega_{\rm shear} = \partial v_z/\partial r$, where r is the radial distance from the jet spine (middle), and the velocity power spectrum of turbulence in the jet-induced flow (bottom).

the details of nonlinear structures, such as, shocks, shear, and turbulence, and hence we have been able to analyze the characteristics of flow structures. For instance, the Mach numbers of shocks have a power-law distribution except the bowshock (see the right-top panel of Figure 2), indicating that most of them are originated from turbulence. Strong shear is generated in the jet and backflow boundary (see the right-middle panel). And the turbulence in the jet-induced flows seems to follow the Kolmogorov spectrum (see the right-bottom panel).

The full description of the jet flow structures is given in Seo et al. (2021b).

This work was supported by the National Research Foundation (NRF) of Korea through grants 2016R1A5A1013277, 2020R1A2C2102800, and 2020R1F1A1048189. The work of J.S. was also supported by the NRF through grant 2020R1A6A3A13071702. Some of simulations were performed using the high performance computing resources of the UNIST Supercomputing Center.

References

Borges, R., Carmona, M., Costa, B., & Don, W. S. 2008, J. Comput. Phys., 227, 3191
Buchmüller, P., Dreher, J., & Helzel, C. 2016, ApMaC, 272, 460
Buchmüller, P., & Helzel, C. 2014, JSCom, 61, 343
Dumbser, M., Moschetta, J.-M., & Gressier, J. 2004, JCoPh, 197, 647

https://doi.org/10.1017/S1743921322001314 Published online by Cambridge University Press

English, W., Hardcastle, M. J., & Krause, M. G. H. 2016, *MNRAS*, 461, 2025
Fleischmann, N., Adami, S., Hu, X. Y., & Adams, N. A. 2020, JCoPh, 401, 109004
Gottlieb, S. 2005, Journal of Scientific Computing, 25, 10
Hardcastle, M. J. & Croston, J. H. 2020, *New Astron. Revs*, 88, 101539
Jiang, G.-S., & Shu, C.-W. 1996, J. Comput. Phys., 126, 202
Jiang, G.-S., & Wu, C.-C. 1999, J. Comput. Phys., 150, 561
Landau, L. D., & Lifshitz, E. M. 1959, Fluid mechanics
Li, Y., Wiita, P. J., Schuh, T., et al. 2018, *ApJ*, 869, 32
Liu, X.-D., Osher, S., & Chan, T. 1994, J. Comput. Phys., 115, 200
Liu, S., Shen, Y., Zeng, F., & Yu, M. 2018, International Journal for Numerical Methods in Fluids, 87, 271
Mathews, W. G. 1971, *ApJ*, 165, 147
Matthews, J. H., Bell, A. R., Blundell, K. M., et al. 2019, *MNRAS*, 482, 4303
Martí, J. M. & Müller, E. 2003, Living Reviews in Relativity, 6, 7
Martí, J. M. & Müller, E. 2015, Living Reviews in Computational Astrophysics, 1, 3
Mignone, A., Plewa, T., & Bodo, G. 2005, *ApJS*, 160, 199
Peery, K., & Imlay, S. 1988, in 24th Joint Propulsion Conf. (Reston, VA:AIAA Journal), 2904
Ryu, D., Chattopadhyay, I., & Choi, E. 2006, *ApJS*, 166, 410
Seo, J, Kang, H., & Ryu, D. 2021b, *ApJ*, 920, 144
Seo, J, Kang, H., Ryu, D., Ha, S., & Chattopadhyay, I. 2021a, *ApJ*, 920, 143
Shu, C.-W., & Osher, S. 1988, J. Comput. Phys., 77, 439
Shu, C.-W., & Osher, S. 1989, J. Comput. Phys., 83, 32
Spiteri, R. J., & Ruuth, S. J. 2002, SIAM Journal on Numerical Analysis, 40, 469
Spiteri, R. J., & Ruuth, S. J. 2003, Mathematics and Computers in Simulation, 62, 125
Synge, J. L. 1957, The Relativistic Gas, Series in Physics (Amsterdam: North-Holland)
Taub, A. H. 1948, Phys. Rev., 74, 328

https://doi.org/10.1017/S1743921322001314 Published online by Cambridge University Press